frontiers | Frontiers in Earth Science

ORIGINAL RESEARCH
published: 01 July 2022
doi: 10.3389/feart.2022.921995

Bottom Drag Variations Under Waves and Currents: A Case Study on a Muddy Deposit off the Shandong Peninsula

*Fukang Qi[1], Zhiqiang Liu[1,2] and Jingping Xu[1,2]**

[1]Department of Ocean Science and Engineering, Southern University of Science and Technology, Shenzhen, China, [2]Southern Marine Science and Engineering Guangdong Laboratory (Guangzhou), Guangzhou, China

Bottom drag coefficient is one of the key parameters in quantifying shelf hydrodynamics and sediment transport processes. It varies markedly due to dynamic forcing and bed type differences, so a set of empirical values have been used for beds of coarse material where bedforms are often present. In comparison, dramatically fewer such rule-of-thumb values are available for muddy beds. Here, we present results of variations in bottom drag as calculated from *in situ* measurements by bottom-mounted tripods that were placed across the top of a muddy deposit during two different deployments, one in summer and another in winter. A tidal asymmetry of bottom drag was observed, most likely caused by variations of local bed roughness. For hydrodynamically smooth ($Re < 2.3 \times 10^5$) flows, computed values of bottom drag coefficient were fairly scattered but still showed an overall decreasing trend with an increase in Reynolds number. The bottom drag coefficient for hydrodynamically rough or transitional flow was typically constant, while the averaged drag coefficient over all observation periods was 1.7×10^{-3}. Smaller waves (bottom orbital velocity u_b <0.1 m/s) had a very limited impact on the bottom drag coefficient. However, with an increase in u_b, the wave–current interactions can decrease the time-averaged near-bed velocity and enhance turbulent kinetic energy, thus leading to an increase in the drag coefficient.

Keywords: continental shelf, drag coefficient, muddy deposit, tidal asymmetry, wave–current interaction

Edited by:
Ya Ping Wang,
East China Normal University, China

Reviewed by:
Qian Yu,
Nanjing University, China
Junbiao Tu,
Tongji University, China

****Correspondence:***
Jingping Xu
xujp@sustech.edu.cn

Specialty section:
This article was submitted to Geohazards and Georisks, a section of the journal Frontiers in Earth Science

Received: *17 April 2022*
Accepted: *12 May 2022*
Published: *01 July 2022*

Citation:
Qi F, Liu Z and Xu J (2022) Bottom Drag Variations Under Waves and Currents: A Case Study on a Muddy Deposit off the Shandong Peninsula. Front. Earth Sci. 10:921995. doi: 10.3389/feart.2022.921995

INTRODUCTION

Within the bottom boundary layer (BBL) on an oceanic shelf, bottom friction changes the velocity profile of the flow and the production/dissipation of turbulence, thus affecting the processes of physical, biological, chemical, and sediment transport (Trowbridge and Lentz, 2018). Among the numerous hydrodynamic and sediment dynamic models (Fringer et al., 2019), the current-related bed shear stress, τ_c, is commonly parameterized with the quadratic drag-law:

$$\tau_c = \rho C_D \bar{u} |\bar{u}|, \tag{1}$$

where ρ is the water density, $\bar{u}$ is the near-bed burst mean current velocity, and C_D is the bottom drag coefficient. In a current BBL (without waves and unstratified), the near-bed current velocity is usually represented by the logarithmic law of the wall (log-law):

$$\bar{u}(z) = \frac{u_{*c}}{\kappa} ln\left(\frac{z}{z_0}\right), \tag{2}$$

where u_{*c} ($\sqrt{\tau_c/\rho}$) is current-related frictional velocity, κ = 0.40 is the von Kármán constant, and z_0 is hydrodynamic roughness length, which is commonly a function of grain size, bedforms, and sediment motion (Xu and Wright, 1995; Trembanis et al., 2004). Combining **Eqs. 1**, **2**, we can deduce that the value C_D depends upon z_0 (e.g., Soulsby, 1997; Feddersen et al., 2003). Regions of sandy deposits with ripples or sand waves C_D could be well estimated by z_0 assuming the anisotropy of bedforms is appropriately quantified with sufficient spatiotemporal resolution (Scully et al., 2018). Unlike sandy deposits, sediments in muddy deposits usually exhibit cohesive properties that hinder the development of bedforms such as ripples (Baas et al., 2019). In the research practice of hydrodynamics, C_D is usually assumed to be a constant or a tuning parameter in the muddy areas (e.g., Harris and Wiberg, 2001; Magaldi et al., 2009). However, numerous observational studies have shown that C_D varies with waves, currents, biological conditions, and stratifications (e.g., Herrmann and Madsen, 2007; Safak, 2016; Xu et al., 2017; Egan et al., 2020a).

In the shallow water of continental shelves, the presence of surface waves (therefore wave-current interaction) impacts the hydrodynamics of the centimeter-scale wave BBL as well as the entire water column (Grant and Madsen, 1986). Wave actions change the velocity structure within the BBL and cause the flow to experience stronger drag (Grant and Madsen, 1979; Signell and List, 1997; Styles and Glenn, 2000; Nayak et al., 2015; Egan et al., 2019), but a recent study by Nelson and Fringer (2018) has shown that waves may lead to a decrease in drag on a smooth bed. Enhanced shear stress by energetic waves often leads to the resuspension of bed sediments (Brand et al., 2010; Egan et al., 2020b), which can further lead to stratification of suspended sediment and the drag-reduction effect on the flow (e.g., Wright et al., 1999; Peng et al., 2020). Therefore, the use of *in situ* data to obtain C_D a certain spatial and temporal resolution is of great importance for hydrodynamic and sediment dynamic studies.

Recent studies on sediment transport processes in the muddy areas of the East China Shelf Seas (ECSS) have often deployed numerical models such as the Regional Ocean Modeling System (e.g., Bian et al., 2013; Liu et al., 2015; Wang et al., 2019; Wang et al., 2020). The Regional Ocean Modeling System implements the simple quadratic drag-law approach for calculating BBL processes that require user input of the drag coefficient (Warner et al., 2008). This is often not an easy task because direct measurements of a drag coefficient are extremely scarce in the muddy areas of the ECSS due to a lack of *in situ* observations. Fan et al. (2019) derived the empirical relationship between C_D both currents and waves based on BBL observations at eight stations scattered over the ECSS, many of which are composed of the sandy sea bottom. To our knowledge, however, there has been no report on whether this empirical relationship also applies to coastal muddy areas of the ECSS.

In this study, a field campaign was conducted to measure the BBL dynamics across the top of a mud deposit off the Shandong Peninsula in the Yellow Sea of China. Reynolds stress, therefore C_D, can be estimated from those direct measurements of flows and turbulences. Our goal is to quantify the temporal and spatial variation C_D across the mud deposit, which is essential to interpreting the sediment transport and deposition patterns that shape the unique, elongated mud deposit. This paper is arranged as follows: This paper is arranged as follows: this *"Introduction"* is followed by *"Study Area"*. *"Materials and Methods"* describes the data and methods used in this study. The time series and tidally averages C_D are presented in *"Results"*. Detailed analyses on flood–ebb asymmetry C_D and the effect of waves are discussed in *"Discussion"*. *"Conclusion"* summarizes the findings in this research.

STUDY AREA

The scene of this study is around the depocenter of a muddy deposit in the coastal seas to the east of the Shandong Peninsula, China (**Figure 1A**). The water depths at the study stations are basically within 40 m, and their specific values are shown in **Table 1**. Previous sedimentary studies suggested that this muddy deposit was formed by sediments sourced from the Yellow River and transported by the Shandong Coastal Currents (SDCC), which flow out of the Bohai Sea to the Yellow Sea around the Shandong Peninsula (**Figure 1A**) (Alexander et al., 1991; Yang and Liu, 2007). Followed the Shepard scheme (Shepard, 1954), the surface sediment in the study area belongs to sandy silt with a mean grain size ranging from 5 to 6 ϕ (Yuan et al., 2020). Moreover, because the mud fraction is more than 10% (Yuan et al., 2020; Qi et al., 2022), the bed sediment may have significant cohesive properties (Bass et al., 2002; Van Rijn, 2007). In the Yellow Sea, the principal tidal constituent is M_2, followed by S_2 and K_1 (Teague et al., 1998). The hydrography of the Yellow Sea is also influenced by the seasonally varied East Asian Monsoon (Naimie et al., 2001). In summer, the southerly winds dominate the wind field, and in winter, strong northerly winds generally prevail over the Yellow Sea (Bian et al., 2013; Mo et al., 2016; Wang et al., 2020).

MATERIALS AND METHODS

Data Collection

Tripods were deployed at three stations on the Inner Shelf of the Shandong Peninsula during two 10-day field campaigns, one in summer (August 18–27, 2017), and another in winter (February 23–March 2, 2018) (**Figure 1B**). One more winter deployment (January 6–26, 2020) was conducted to make up for a fallen instrument at S2 during a previous deployment. Each tripod was equipped with an upward-looking Teledyne/RDI 600 kHz Acoustic Doppler Current Profiler (ADCP), a Nortek Vector Acoustic Doppler Velocimeter (ADV), a conductivity/temperature (CT) sensor, and a turbidity sensor (OBS or RBR-TU) (**Table 1**). The sampling period of each instrument is shown in **Table 1**. In addition, for winter observations at S2, turbidity sensors were placed at 0.45, 0.9, and 1.34 m above the bottom (mab) to record sediment concentrations within the bottom boundary layer (**Table 1**). CTD (SeaBird 19) packaged with Niskin bottles and a turbidity sensor was cast to collect water samples and profiles of temperature, salinity, and turbidity periodically from the watching boats that guarded each

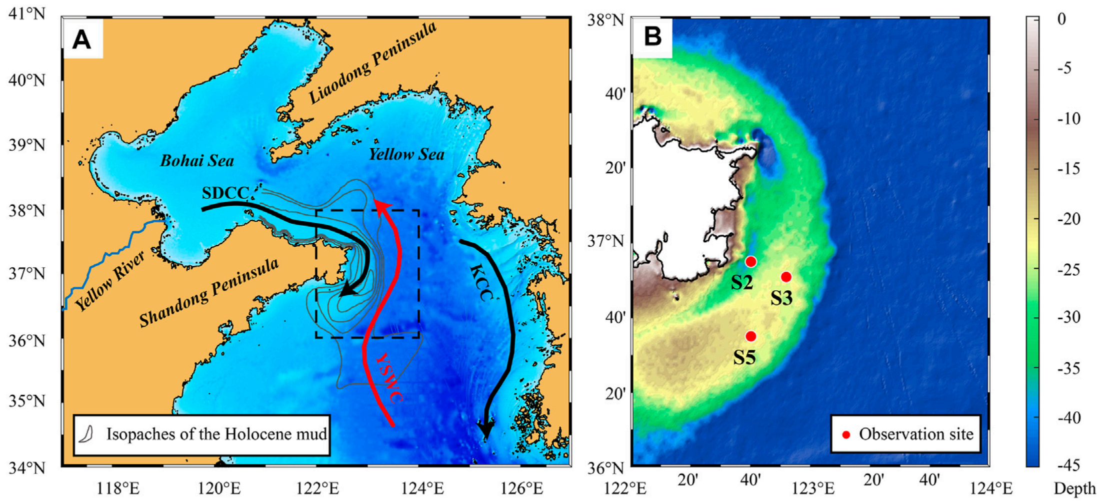

FIGURE 1 | (A) Topography and currents of the Bohai and Yellow seas. The isopaches of the muddy area were from Yang and Liu (2007), and the currents were based on Bian et al. (2013). These currents are the Shandong Coastal Current (SDCC), the Yellow Sea Warm Current (YSWC), and the Korea Coastal Current (KCC) **(B)** The location of the observation sites.

TABLE 1 | Mean water depth and settings of six observations.

Label	Depth (m)	Instruments	Mab	Sampling
S2 summer	40.1	ADCP	1.8	20 min (currents), 1 h (waves)
		ADV	0.67	1/32 s
		RBR-CT	1.1	3 s
		OBS	1.1	40 s
S3 summer	26.5	ADCP	1.5	10 min
		ADV	0.4	1/32 s
		RBR-CT	0.88	3 s
		OBS	0.88	1 min
S5 summer	23.3	ADCP	1.7	10 min
		ADV	0.48	1/32 s
		RBR-CT	1.15	3 s
		RBR-TU	1.15	3 s
S2 winter	38.9	ADCP	1.7	2 min (currents), 1 h (waves)
		ADV	0.6	1/32 s
		RBR-CT	0.83	10 s
		RBR-TU	0.45, 0.9, 1.34	3 s, 10 s, 3 s
S3 winter	26.6	ADCP	1.9	20 min (currents), 1 h (waves)
		ADV	0.88	1/32 s
		RBR-CT	1.16	10 s
		RBR-TU	1.16	10 s
S5 winter	23.3	ADCP	1.85	20 min (currents), 1 h (waves)
		ADV	0.84	1/32 s
		RBR-CT	1.2	10 s
		RBR-TU	1.2	10 s

Teledyne/RDI Acoustic Doppler Current Profiler (ADCP, 600 kHz); Nortek Vector Acoustic Doppler Velocimeter (ADV); Conductivity/temperature sensor (CT); Turbidity sensor (OBS or RBR-TU). Sites S2, S3, and S5 are mapped in ***Figure 1****.*

instrument against being damaged by trawling nets of passing fishing boats. These water samples were used to calibrate and convert the observed turbidities into suspended sediment concentrations (SSCs). Detailed processes of data quality assurance/quality control and calibration can be found in Qi et al. (2022).

Most ADCPs are equipped with a waving module that enables wave measurements (**Table 1**). In addition, hourly significant wave height and wave period data from the WaveWatch III Global Wave Model (WW3) at approximately 0.5° (~50 km) resolution (Tolman et al., 2014), is widely used in coastal studies (e.g., Duan et al., 2020; Silva et al., 2018), were downloaded. We compared the modeled and observed significant wave height (H_s) and peak wave period (T_p) at Site 3 (S3) in winter to verify the validity of the model, and the results

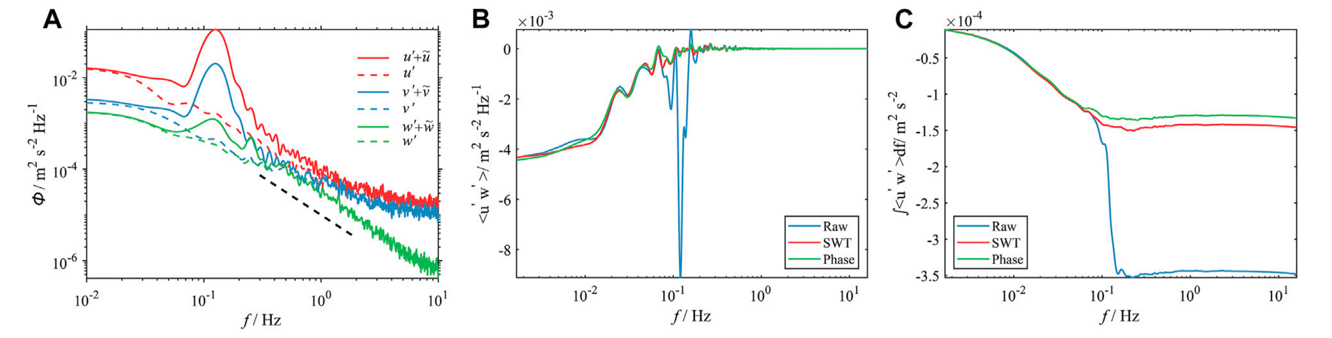

FIGURE 2 | (A) Power spectra of velocity fluctuation and turbulent fluctuation (u', v' and w') estimated by Phase method for burst 41 of S3 winter observation. **(B)** Cospectra and **(C)** accumulative cospectra of raw velocity fluctuation and turbulent fluctuations estimated by these two methods.

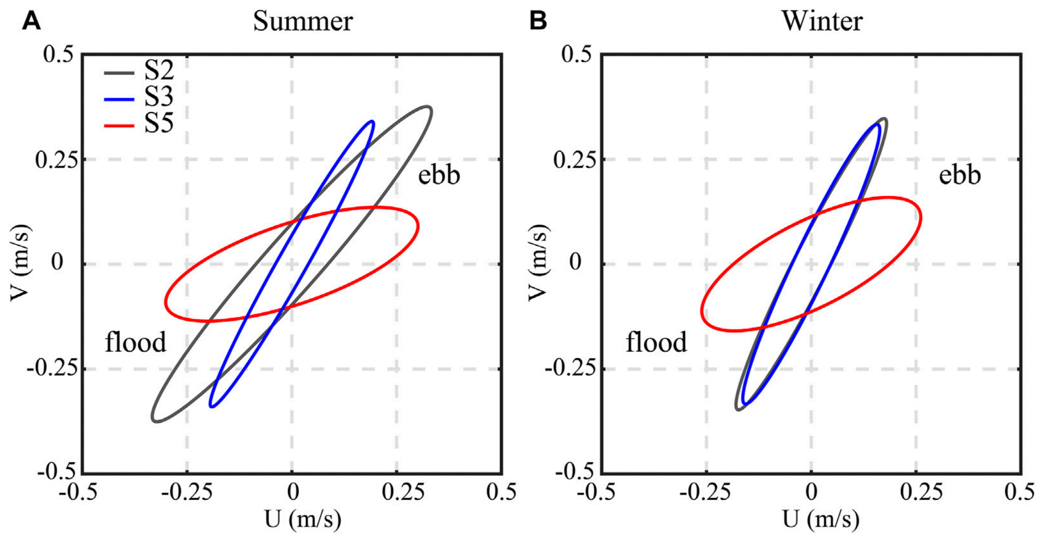

FIGURE 3 | Tidal ellipses of M_2 tidal components were calculated from the mean velocity at 1 mab in **(A)** summer and **(B)** winter for each of the three stations. The mean velocity was translated from ADV data by log law.

showed that both of them have a strong relationship, with a correlation coefficient $R = 0.95$ and 0.91, respectively (**Supplementary Figure S1**). Wind data were downloaded from the National Enters for Environmental Prediction Climate Forecast System Version 2 (NCEP/CFSv2) with a horizontal resolution of $0.205^\circ \times 0.204^\circ$ (Saha et al., 2014).

Tidal Analysis and Wave Parameter Estimates

We used T_TIDE, a package of routines in MATLAB for harmonic analysis, to make a tidal prediction (Pawlowicz et al., 2002). In agreement with previous studies, the dominant tidal constituent was M_2, flowing southwest during flood tide and northeast during ebb tide.

The bottom wave orbital velocity, u_b, was estimated following Van Rijn (1993):

$$u_b = \frac{\pi H_s}{T_p\, shih\,(k \cdot h)}, \tag{3}$$

where H_s is the significant wave height, T_p is the peak wave period. k ($= 2\pi/L$, where L is wavelength) is the wavenumber. Soulsby (2006) Newton–Raphson method was used to calculate wavenumbers, and the MATLAB function for this method could be found in Wiberg and Sherwood (2008). h is water depth.

Wave–Turbulence Decomposition and Turbulence Quantities

In a wavy aquatic environment, the ADV measured velocity components (u, v, and w) can be decomposed into the mean, wave, and turbulent fluctuation components. Before analysis, the horizontal velocities were rotated into a streamwise orthogonal coordinate system with u v components aligned with and orthogonal to the direction of the mean flow. Take u as an example, $u = \bar{u} + \tilde{u} + u'$, where $\bar{u}$ the burst mean velocity averaged per 10 min, $\tilde{u}$ is the wave component and u_t' is the turbulent fluctuation. Assuming that waves and turbulence are uncorrelated (i.e., terms such as $\overline{u'\tilde{w}}$ vanish), the shear stress can be decomposed into turbulent and wave components:

$$\text{Total shear stress} = -\overline{u'w'} - \overline{\tilde{u}\tilde{w}}, \tag{4}$$

where $-\overline{u'w'}$ is the turbulent Reynolds stress and $-\overline{\tilde{u}\tilde{w}}$ is the wave momentum flux (wave stress). To obtain an accurate estimate of Reynolds stress, here we used the "Phase method" of Bricker and Monismith (2007) for the wave-turbulence decomposition (WTD). As shown in **Figure 2**, the Phase method can effectively remove the wave motions.

Following Feddersen and Williams (2007), we used the nondimensional integrated cospectrum (ogive) for controlling the quality of WTD and the Reynolds stress estimates. The ogive for $\overline{u'w'}$ is defined as

$$Og_{u'w'}(f) = \frac{\int^{f} Co_{u'w'}(\hat{f})d\hat{f}}{\langle u'w' \rangle}, \tag{5}$$

where $Co_{u'w'}$ is the $u'w'$ cospectrum. After removing the wave bias, the $Og(f)$ curves are expected to increase smoothly from 0 to 1 in the range $10^{-1} < 2\pi fzu < 10$ (Feddersen and Williams, 2007), similar to empirical curves proposed by Kaimal et al. (1972). Following Ruessink (2010), we applied the ogive acceptance range as: $-0.3 < Og(f) < 1.3$, where estimates outside of this range were eliminated. In addition, referring to Tu et al. (2021), we compared the observed ogive curves $\overline{u'w'}$ in the empirical form and rejected those that were not well fitted. The ogive test excluded 8.5–29.7% of the bursts from each deployment (**Supplementary Table S1**).

After obtaining the turbulent fluctuation in three directions, we calculated the Reynolds stress, turbulent kinetic energy (TKE), and turbulent energy dissipation rates (ε). The TKE was estimated as: $1/2\rho(\overline{u'^2} + \overline{v'^2} + \overline{w'^2})$. The inertial dissipation method was used to calculate the turbulent energy dissipation rates (Liu and Wei, 2007):

$$\varepsilon = 2\pi U^{-1}\alpha_3^{-3/2}\overline{\left[f^{5/2}\phi_{w'}^{3/2}(f)\right]}, \tag{6}$$

where U is the mean velocity of each burst, $\alpha_3 \approx 0.71$ is the Kolmogorov constant (Sreenivasan and Katepalli, 1995), f is the frequency of the inertial subrange, which is approximately 1–3 Hz here (**Figure 2**), and $\phi_{w_t'}$ is the frequency spectrum density of the w component over the inertial subrange.

Calculation of the Bottom Drag Coefficient

The Bottom drag coefficient was estimated following Egan et al. (2020a). As $\tau_c = -\rho\overline{u'w'}$, we rearranged **Eq. 1** and obtained

$$C_D = \frac{-\overline{u'w'}}{\bar{u}|\bar{u}|}. \tag{7}$$

The instantaneous C_D can be directly calculated by **Eq. 7**, and the C_D in a certain range of conditions (e.g., flood and ebb tide) can be estimated as the best-fit slope from a least-squares regression of the two terms on the right-hand side of **Eq. 7**. For the convenience of comparing C_D at different sites, we applied the log-law to deduce mean velocity at 1 mab ($\bar{u}_{100}$) during weak waves and unstratified periods. Based on **Eq. 2**, the mean current velocity at the reference height (1 mab) can be expressed as $\bar{u}_{100} = u(z) + (u_{*c}/\kappa)ln(1/z)$. C_{100} represents the drag coefficient calculated at 1 mab. As the calculation C_D is based on the assumption that the measuring volume is within the constant stress layer which is ~10–30% of the BBL thickness (δ) (Soulsby, 1997), we calculated δ using the equation (Soulsby, 1983): $\delta = 0.44u_{*c}/f$, where f is the Coriolis parameter, and retained data for δ greater than 10 m. The calculation results show that more than 99.8% of the bursts satisfy this condition.

Combining **Eqs. 1**, **2**, we can deduce the dependence of C_D on z_0:

$$C_D = \left[\frac{1}{\kappa}ln\left(\frac{z}{z_0}\right)\right]^{-2}. \tag{8}$$

RESULTS

Tides, Currents, Waves, and Winds

Figure 3 shows the tidal ellipses of M_2 tidal components in summer and winter for each of the three stations. According to the rotation rate of the tidal ellipse, tide currents in sites S2 and S3 were reversing currents, while the tide in Site 5 (S5) was rotary currents (**Figure 3**). The maximum tidal velocity had a certain difference for each site, and was generally satisfied: S2>S3>S5, where the maximum tidal velocity of S2 was approximately 0.5 m/s (**Figure 3**).

Figure 4 shows the magnitude of wave orbital velocities and wave directions. The maximum value of wave orbital velocity in summer was about 0.12 m/s (**Figure 4A**), and the average values were 0.01 m/s, 0.03 m/s, and 0.04 m/s at S2, S3, and S5, respectively. The wave propagation was mainly in the northwesterly direction in summer. It was not exactly matching with the direction of the instantaneous winds (**Figure 5A**) but was consistent with the trend of the prevailing southerly winds (Wu et al., 2019), indicating that the swell waves and background flow dominated the wave propagation.

The overall intensity of waves was significantly higher in winter than that in summer (**Figure 4**). The maximum value of wave orbital velocity in winter was about 0.37 m/s, and the average values at S2, S3, and S5 were 0.01 m/s, 0.05 m/s, and 0.06 m/s, respectively. The wave direction was modulated by the local wind field. During periods of weak wind (wind speed less than 10 m/s), the wind direction was not fixed and was dominated alternately by southwesterly and northeasterly winds (**Figure 5B**). Therefore, when the orbital velocity was smaller than 0.1 m/s, the wave propagation direction was mainly southwestward or northeastward (**Figure 4B**). However, the stronger wind events (wind speed greater than 10 m/s) that occurred during the observation period were dominated by northerly winds (**Figure 5B**). Therefore, the wave propagation direction was mainly southwesterly when the orbital velocity was greater than 0.1 m/s (**Figure 4B**). Wave orbital velocities were higher

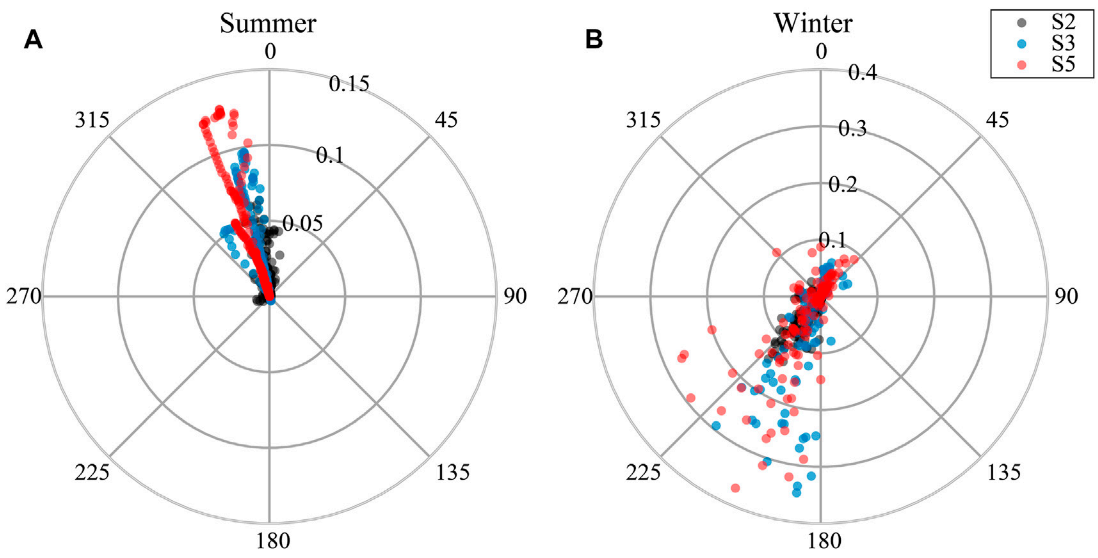

FIGURE 4 | Wave magnitude and direction for three stations (S2, S3, and S5) in **(A)** summer and **(B)** winter, with 0° corresponding to the northward propagating wave, and the radial axis representing the bottom wave-orbital velocity, u_b, in m/s.

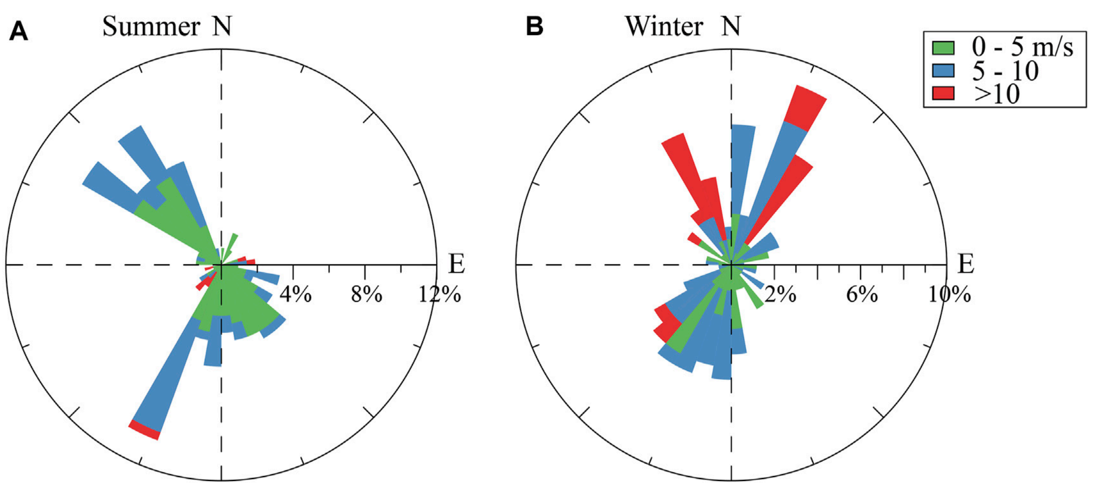

FIGURE 5 | Rose diagrams of hourly averaged wind frequencies during **(A)** summer and **(B)** winter observations at S3. The greyscale indicates the categories of wind speed (m/s).

at S3 and S5 than that at S2 because of the shallower water depth (**Table 1**). We used data in winter to discuss wave-current interactions in the rest of the article.

Bottom Drag Coefficient

First, we estimated time-series C_D values at the three stations during both summer and winter deployments. In summer, C_D varied from 5×10^{-4} to 10^{-2} at all stations, with most of it between 10^{-3} and 2×10^{-3} (**Figure 6**). In winter, C_D varied from 10^{-3} to 10^{-2} at S3 and S5, with most of it between 10^{-3} and 3×10^{-3} (**Figure 7**). At S2 in winter, the range C_D was the same as S3 and S5 before January 18. However, after 18 the maximum C_D extent to 10^{-1} (**Figure 8B**). From the time series data, we found that a sudden increase of the near-bottom SSC occurred around 08:00 on January 18 of the winter observation at S2 (**Figure 8C**). Thus, we divided the data into two periods: calm and event periods (**Figure 8**). The probable reason for this event will be discussed in the following part. Moreover, we found that C_D showed varying degrees of flood–ebb tidal asymmetry during the different observation periods. For example, at S3 in summer, the C_D values during ebb tides were larger than those during flood tides (**Figure 6D**). However, this relationship was not fixed between observations at different stations or even at the same station in different seasons. For example, station S2 had a larger

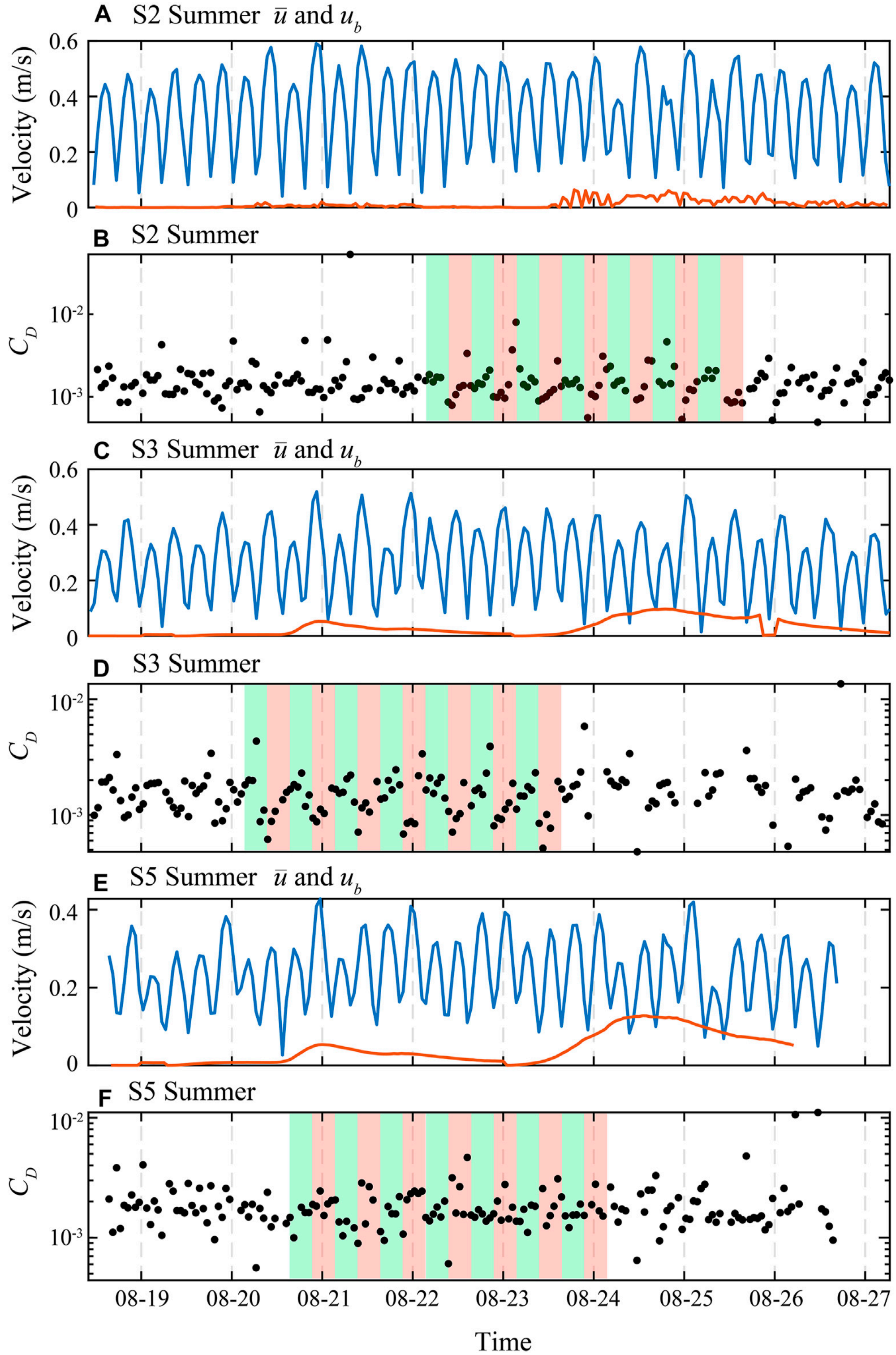

FIGURE 6 | Time series of **(A,C,E)** ADV's burst mean velocity ($\bar{u}$, blue line) and bottom wave orbital velocity (u_b, orange line) and **(B,D,F)** drag coefficient, C_D, estimated using ADV's burst mean velocity at S2, S3, and S5 in summer. Green and red shaded areas denote periods of ebb and flood tides, respectively.

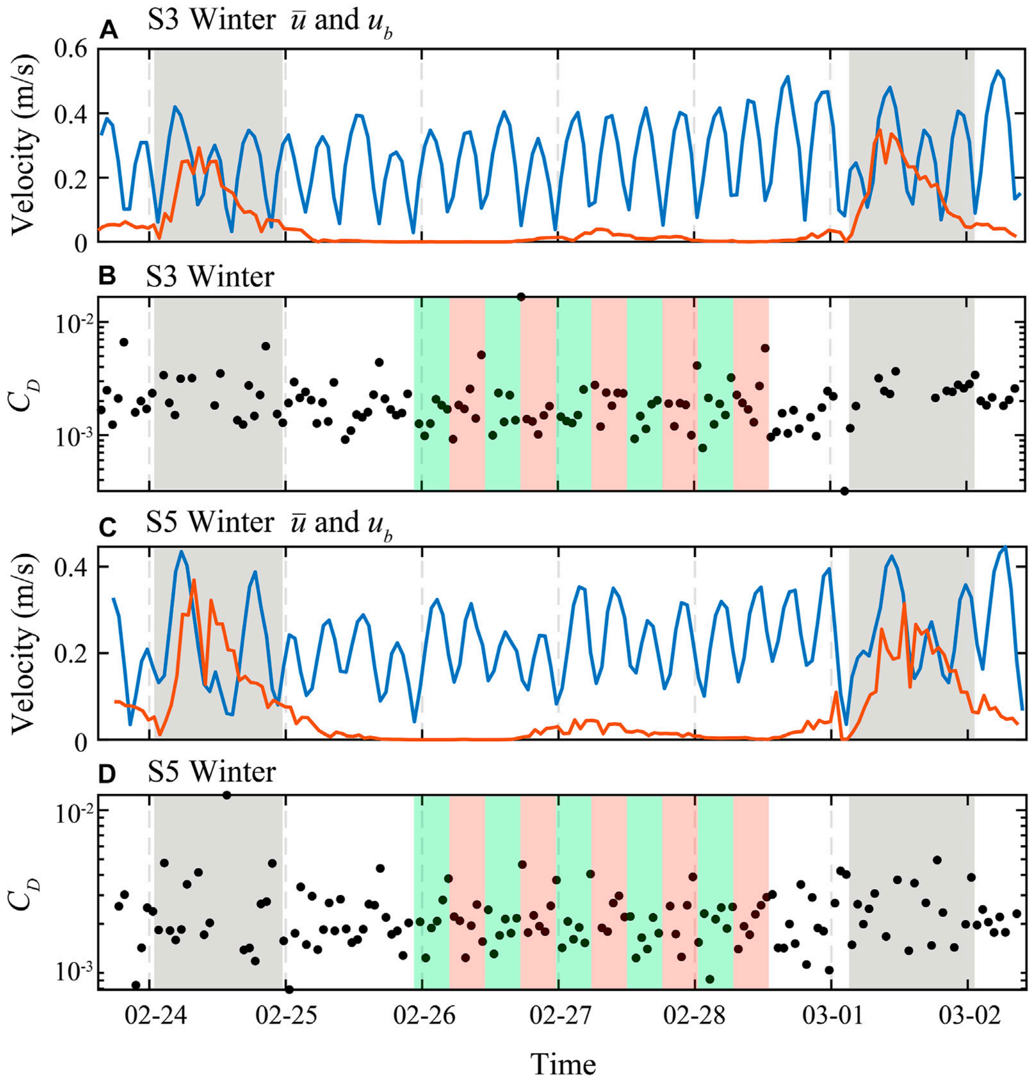

FIGURE 7 | Time series of **(A,C)** ADV's burst mean velocity ($\bar{u}$, blue line) and bottom wave orbital velocity (u_b, orange line) and **(B,D)** drag coefficient, C_D, estimated using ADV's burst mean velocity at S3 and S5 in winter. Green and red shaded areas denote periods of ebb and flood tides, respectively, and gray shaded areas denote periods of strong winds.

C_D ebb tide in summer (**Figure 6B**) and a larger C_D flood tide in winter (**Figure 8B**). Moreover, after the event, C_D increased significantly during flood tides, while the change C_D during ebb tides was relatively small (**Figure 8B**). In addition, the fluctuation C_D in summer followed the tidal cycle variation of flow velocity while the effect of waves was weak (**Figure 6**). But in winter, affected by stronger waves, C_D during the wind events were relatively larger than that during calm periods at all three stations (**Figures 7,8A,8B**).

To recognize the flood–ebb tidal asymmetry C_D and compare C_D at different sites, C_{100} flood or ebb tides at each station were estimated using least-squares regression (**Figure 9**). Note that only data during calm periods (with weak waves and no sediment stratification) are shown in **Figure 9** to ensure the feasibility of log law. Generally, C_{100} ranged from 0.0010 to 0.0020 (average, 0.0015 ± 0.0004) in summer and from 0.0013 to 0.0026 (average, 0.0019 ± 0.0005) in winter. There was little difference estimated C_D between summer and winter at S5. However, at S2 and S3, the C_D in winter was twice that in summer during the flood tide, while the estimated C_D did not show extensive differences during the ebbing tide in summer and winter. The R^2 of the fitted curves for each observation was above 0.71 except for the C_D S2 in winter. At S3 in summer and at S2 in winter, C_D a significant flood–ebb tidal asymmetry, and its controlling factors are discussed in **Section 5**.

DISCUSSION

Variation of C_D During an S2 Winter Event

During event periods, the SSC at 0.45 mab was significantly higher than that of 1.34 mab, which caused significant suspended

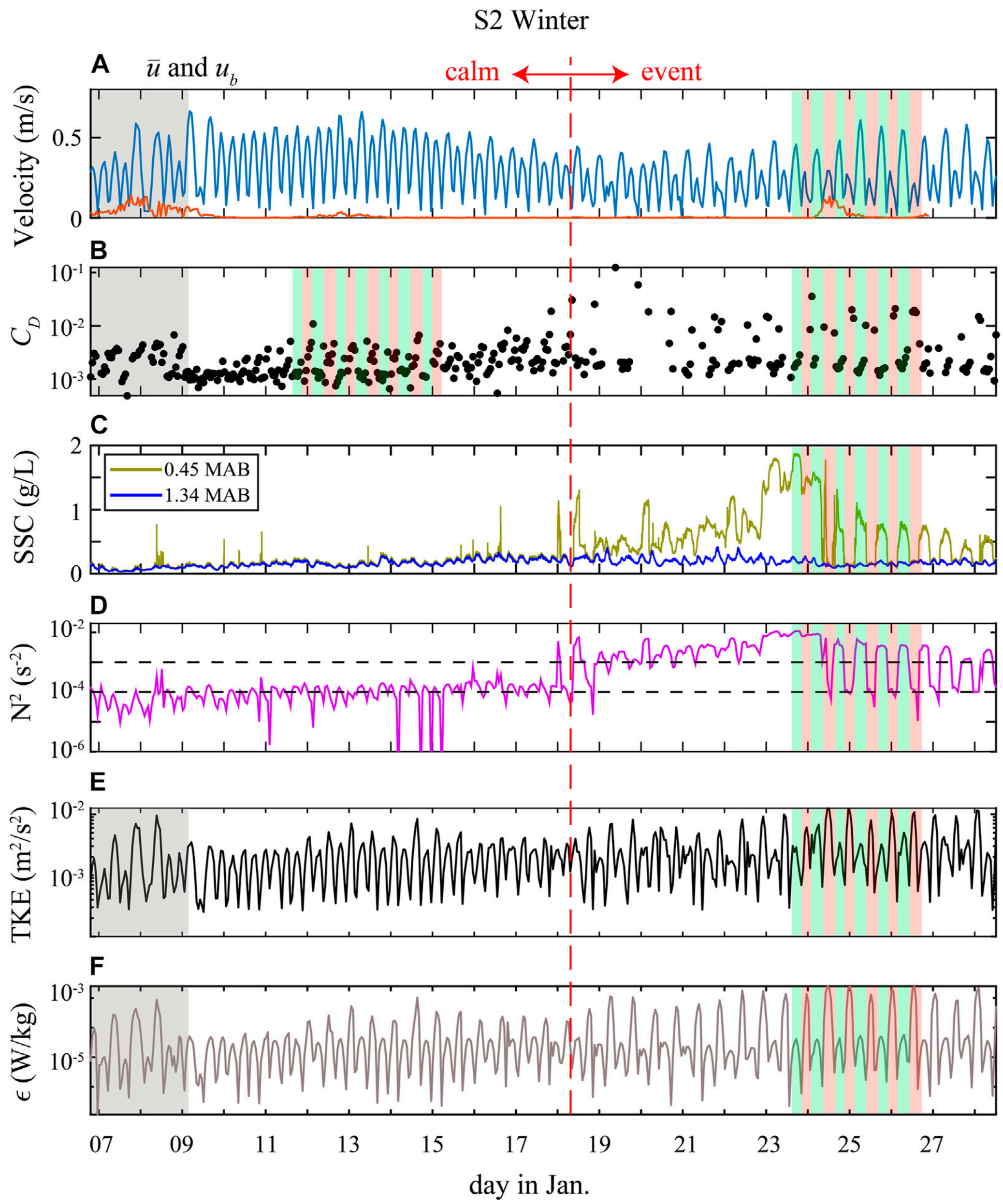

FIGURE 8 | Twenty-day time series during the winter deployment at S2 showing measurements of **(A)** ADV's burst mean velocity ($\bar{u}$, blue line) and bottom wave orbital velocity (u_b, orange line), **(B)** drag coefficient, C_D, estimated using ADV's burst mean velocity, **(C)** suspended sediment concentration (SSC) at 0.45 mab (yellow line) and 1.34 mab (blue line), **(D)** buoyancy frequency (N^2) and the black dashed line indicates N^2 is equal to 10^{-3} s^{-2}, and 10^{-4} s^{-2}, **(E)** turbulent kinetic energy (TKE) and **(F)** turbulence dissipation rates (ϵ). Green and red shaded areas denote periods of ebb and flood tides, respectively, and gray shaded areas denote periods of strong winds. The vertical red dashed line is the demarcation between the calm and event periods.

sediment stratification (**Figure 8C**). We used the buoyancy frequency squared, $N^2 = -\frac{g}{\rho_0}\frac{\partial\bar{\rho}}{\partial z}$, to quantify the magnitude of density stratification (**Figure 8D**). Jones and Monismith (2008) and MacVean and Lacy (2014) took $N^2 = 10^{-4}$ s^{-2} it as the threshold for sediment stratification. Also by comparing gradient Richardson numbers, Peters (1999) showed the critical N^2 of stratification probably be 10^{-3} s^{-2}. In our study, N^2 fluctuated mainly around two typical values, i.e. about 10^{-4} during the calm period and exceeding 10^{-3} during a significant portion of the event period (**Figure 8D**). To facilitate the discussion of stratification, we took $N^2 = 10^{-3}$ s^{-2} it as the threshold for sediment stratification. The results showed that sediment stratification mainly occurred during the ebb tides, especially after January 24, and SSC showed significant tidal asymmetry, i.e., the concentration was not stratified during the flood tides but stratified during the ebb tides. At the same time, the current velocity also showed asymmetry (**Figure 8A**). During the calm period (except for January 9 when S2 was affected by

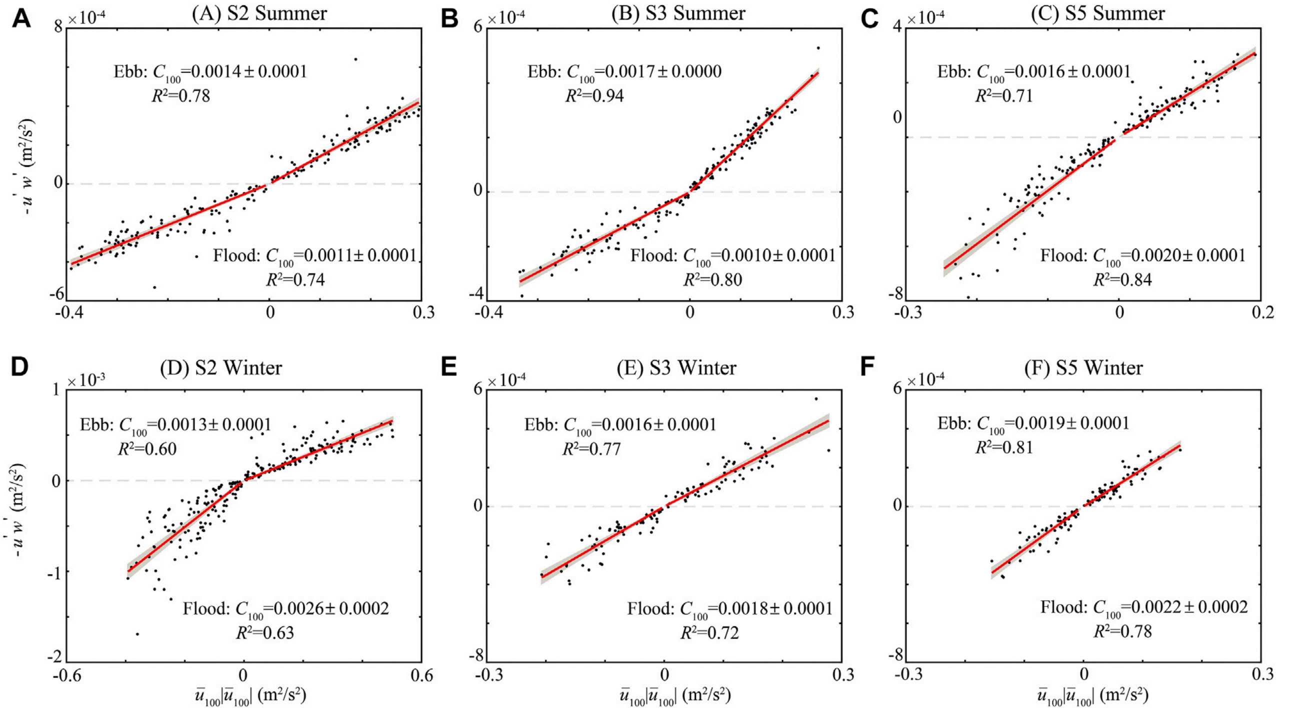

FIGURE 9 | Correlation between measured turbulent Reynolds stress, $-\overline{u'w'}$, and the sign-preserving squared mean velocity at 1 mab, $\bar{u}_{100}|\bar{u}_{100}|$, for the **(A,B,C)** summer and **(D,E,F)** winter. Note that only data during calm periods (with weak waves and no sediment stratification) are shown to ensure the feasibility of log law. The best fit lines are shown in red, with the slopes indicating the drag coefficient, C_{100}, for ebb tides (top) and flood tides (bottom). The 95% confidence intervals (gray shaded areas) and R^2 are shown for each regression.

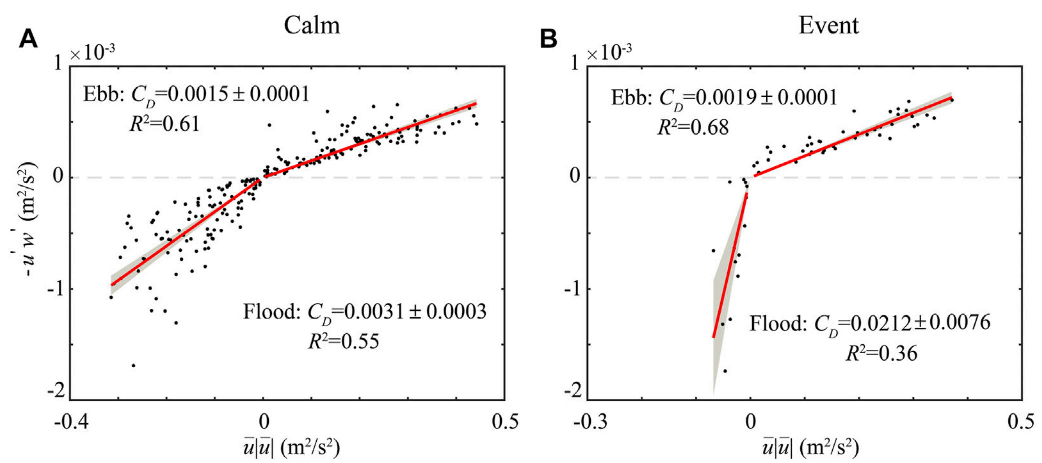

FIGURE 10 | Correlation between measured turbulent Reynolds stress, $-\overline{u'w'}$, and the sign-preserving squared ADV's burst mean velocity, $\bar{u}|\bar{u}|$ at S2 during winter observation. **(A)** Calm period with time before January 18, **(B)** event period after 12:00 on January 24.

strong winds), the current velocities of flood and ebb tides were similar. In contrast, during the event period, the velocity of the flood tides was significantly smaller than that of the ebb tides (**Figure 8A**).

Figure 10 shows the estimated C_D for two periods. Possibly due to enhanced noise contamination in the water column (Ruessink, 2010; Tu et al., 2021), there were few valid Reynolds stress estimates at the beginning of the event period and we only plotted data after 12:00 on January 24 (**Figure 10B**). For ebb tides, stronger stratification was observed during the event period. Previous studies have shown that sediment stratification could suppress turbulence and reduce the bottom

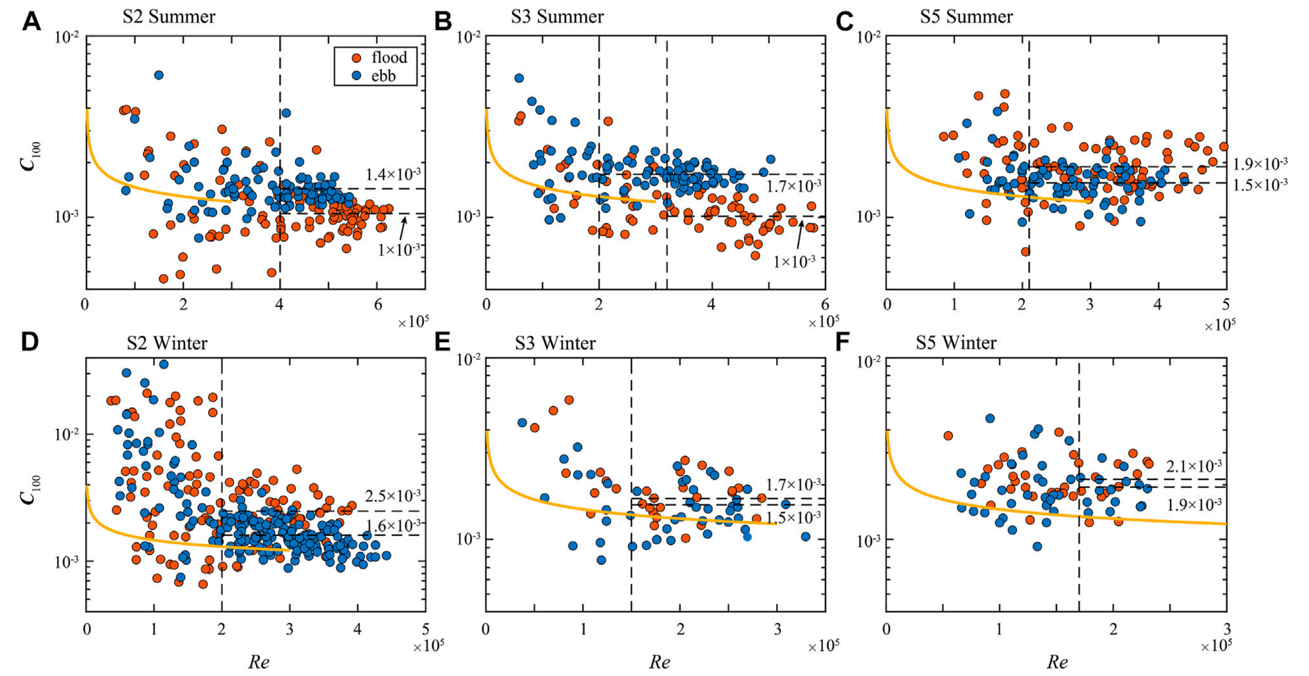

FIGURE 11 | Scatter plots of drag coefficient estimated at 1 mab, C_{100}, versus the Reynolds number (*Re*) for the **(A,B,C)** summer and **(D,E,F)** winter. The orange scatters represent the flood tide, and the blue scatters represent the ebb tide. The vertical dashed lines are the boundary between regions of relatively large and small dispersion. The horizontal dashed lines are the mean value of C_D the right-hand side of the boundary. The yellow lines are the empirical relationship under the assumptions for smooth flow.

drag (Adams and Weatherly, 1981; Tu et al., 2019; Wu et al., 2022). However, when comparing data from before and after the event, estimations C_D were generally the same during ebb tides (**Figure 10**). In addition, TKE and turbulent dissipation rates were also not controlled by stratification even from January 23 to 24, when sediment stratification was more significant and continuous (**Figures 8E,F**), but followed the asymmetry of the flood and ebb tides (**Figure 8A**). For flood tides, the C_D value during the event period was generally seven times larger than that during the calm period. These results suggest that the effect of stratification on C_D was relatively small and the variation of bed configurations, which increased upstream during flood tides, could be the main reason for the variation C_D. Because the study area was located in a shipping channel with shipping vessels moored for shelter and fishing vessels actively trawling, the actual cause of the bed roughness change remains difficult to determine.

Flood–Ebb Asymmetry of C_D

The variation of C_D could be affected by different factors, such as tidal currents (Wright, 1989; Xu et al., 2017), accelerating/decelerating flow (Soulsby and Dyer, 1981; Wright, 1989), waves (Safak, 2016), stratification (Peng et al., 2020), local bathymetry (Fong et al., 2009), upstream/downstream roughness (Scully et al., 2018), benthic biology (Egan et al., 2020a), and water depth (Wang et al., 2014). These factors can lead to asymmetry C_D by influencing mean current velocity or turbulence. First, changes in water depth between flood and ebb tides were relatively small and not sufficient to alter C_D, and we did not find sufficient substrate organisms to alter drag in several box samples. In addition, we did not observe near-bottom density stratification including temperature, salinity, and SSC in either CTD casts or bottom observations, except for the S2 winter (**Figure 8C**), for which there is still asymmetry C_D in the calm period without sediment stratification (**Figure 10A**). Moreover, it is difficult to explain the asymmetry with seasonal variation based on the wind and wave data. For example, the mean wavelength (L) at S5 during strong wind periods was estimated as 65 m; therefore, the wave base ($L/2$) was significantly larger than the water depth. However, C_D had no significant flood–ebb asymmetry at S5. For S2 and S3, the direction of flood tide coincided with the prevailing winter wind direction and was opposed to the prevailing summer wind, but the current experienced stronger drag during flood tides in winter than in summer, which is contrary to our general understanding. Furthermore, the acceleration/deceleration scale of the flow could be characterized by the time derivative of shear velocity (Soulsby and Dyer, 1981; Wilkinson, 1986). As each flood or ebb tide contains an accelerating and decelerating stage, acceleration and deceleration will only affect the fluctuations within a flood or ebb tide and cannot explain the flood–ebb asymmetry. By comparing phase-averaged tidal height (data not shown), we observed no significant seasonal differences, which indicates the variation in tidal forcing is small between winter and summer (Egan et al., 2020a).

Combined with the above analysis, variation in the tidal asymmetry C_D was most likely caused by the difference

TABLE 2 | The mean value of z_0 for hydrodynamic rough flow for flood and ebb tides in summer and winter.

	Summer			Winter		
	S2	**S3**	**S5**	**S2**	**S3**	**S5**
Flood	4.3e–6	3.5e–6	1.0e–4	3.2e–4	6.2e–5	1.7e–4
Ebb	2.6e–5	6.5e–5	3.9e–5	4.6e–5	3.7e–5	1.1e–4

between upstream and downstream roughness. In order to estimate upstream and downstream roughness, we should first determine the hydrodynamic roughness regimes. Generally, the flow regime in the boundary layer can be classified into smooth, transitional, and rough conditions. Hydrodynamically smooth flow, z_0 reflects only the thickness of the laminar sublayer and is not determined by bed configurations (Chriss and Caldwell, 1982; 1984). Meanwhile, experimental and observational evidence has shown that hydrodynamically rough flow, z_0 and C_D are no longer dependent on flow conditions but are related to bed configurations (Sternberg, 1970; Green and Mccave, 1995). Here, we used the Reynolds number (Re) as a criterion for distinguishing the flow conditions:

$$Re = \frac{u_r z_r}{\upsilon}, \tag{9}$$

where u_r is the velocity at the reference height z_r (= 1 m), and υ is the molecular kinematic viscosity taken as 0.01 cm^2/s in summer (20°C, 32 ‰) and 0.016 cm^2/s in winter (4°C, 32 ‰) (Soulsby, 1997). **Figure 11** shows the estimates C_D as a function of Re. Generally, the dispersion C_D decreased with increase Re. Following Sternberg (1968), using the criterion that C_D is generally a constant, we visually estimated the threshold of hydrodynamically smooth flow (vertical dashed lines in **Figure 11**). The mean value of critical Re was about 2.3×10^5. Unsurprisingly, as Re was less than the threshold (i.e., smooth flow), C_D decreased with increase Re, which is consistent with previous findings (Sherwood et al., 2006; Safak, 2016). We substituted the empirical formula z_0 for smooth flow ($z_0 = 0.11\upsilon/u_*$) (Sternberg, 1968, 1970; Chriss and Caldwell, 1984; Soulsby, 1997) into the log-law and plotted this relationship in **Figure 11** (yellow lines) for comparison. When Re was slightly larger than the threshold, C_D fluctuated around the empirical relationship but did not follow the empirical relationship exactly, which may reflect the characteristics of transitional flow. Because z_0 is a constant for rough flow, we found the estimation z_0 by substituting the mean values of C_D **Eq. 8** (**Table 2**). This shows that the larger the tidal asymmetry C_D, the greater the difference in upstream and downstream roughness, which suggests that varying upstream and downstream roughness is the main reason for the flood–ebb asymmetry of C_D.

Bottom Drag Enhanced by Waves

In addition to the change in roughness, the bottom drag experienced by currents could be enhanced by waves, which do affect the flood–ebb asymmetry C_D. We removed the data during strong waves ($u_b > 0.1$ m/s) in winter (red dots in **Figure 12**) and refitted the data to obtain C_D. After refitting the data of S3, the tidal asymmetry was reduced and the difference C_D between the flood and ebb tides changed from 5×10^{-4} to 2×10^{-4} (**Figure 12B**). After refitting the data of S5, the fitted R^2 during flood tides changed from 0.66 to 0.76 (**Figure 12C**). These findings indicated that stronger waves can have a significant effect on bottom drag at S3 and S5, leading to a bias in the C_D estimates. Because relatively few data are available for strong waves, the re-estimated C_D did not change significantly at S2 (**Figure 12A**).

To quantify the effect of waves, we used a one-dimensional time-dependent model, referred to as the Grant-Madsen (GM) model, that incorporates the combined effects of a steady current in the presence of oscillatory waves (Grant and Madsen, 1979). In the GM model, the friction velocity combined waves and currents (u_{*cw}) is given by

$$u_{*cw} = u_{*w}\left[1 + 2\left(u_{*c}/u_{*w}\right)^2 \cos\phi + \left(u_{*c}/u_{*w}\right)^4\right]^{1/4}, \tag{10}$$

where ϕ is the angle between currents and the direction of wave propagation. In addition, u_{*w} is the friction velocity associated with the wave-related bed shear stress (τ_w) given as

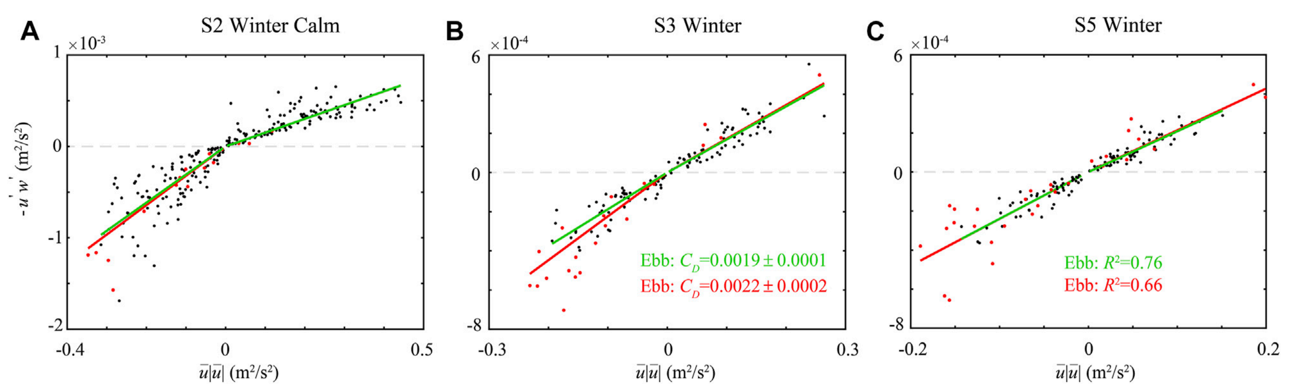

FIGURE 12 | Correlation between measured turbulent Reynolds stress, $-\overline{u'w'}$, and the sign-preserving squared ADV's burst mean velocity, $\bar{u}|\bar{u}|$, for the **(A)** S2 calm period, **(B)** S3, and **(C)** S5 in winter without the strong wave observations (red dots). The best fit lines without the strong wave observations (red dots) are shown in green and the best fit lines of all data are shown in red, with the slopes indicating the drag coefficients, C_D, for ebb tide (top) and flood tide (bottom).

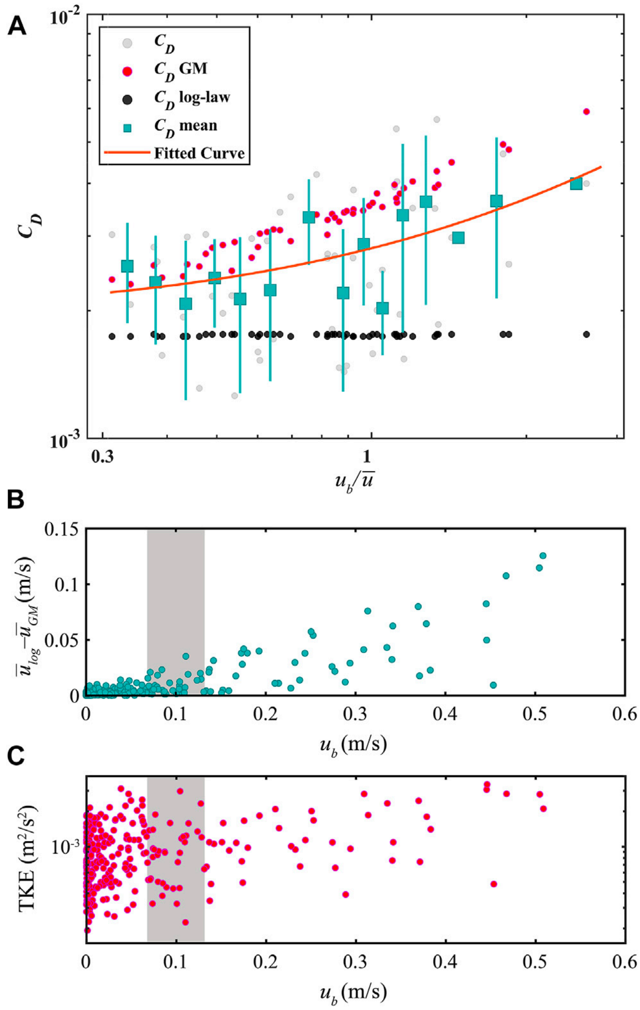

FIGURE 13 | (A) Scatter plots of C_D verses u_b / $\bar{u}$ when u_b > 0.1 m/s for S3 and S5 in winter. Gray dots indicate directly observed C_D, red dots indicate C_D calculated by the Grant-Madsen model, black dots indicate C_D calculated by log-law, blue squares are the bin averages of observed C_D, and vertical lines indicate standard deviation. The best fine line observed C_D is shown in orange. **(B)** The difference $\bar{u}$ calculated by the log-law velocity profile ($\bar{u}_{law}$) and the Grant-Madsen model ($\bar{u}_{GM}$) and **(C)** turbulent kinetic energy (TKE) as a function of u_b.

$$u_{*w}^2 = \frac{\tau_w}{\rho_0} = \frac{\kappa u_{*cw} u_b}{\sqrt{\left[\log\left(\frac{\kappa u_{*cw}}{z_0 \omega}\right) - 1.15\right]^2 + \left(\frac{\pi}{2}\right)^2}}, \quad (11)$$

where ω ($= 2\pi/T_p$) is the wave frequency. Here, we assumed $z_0 = 2 \times 10^{-5}$ m, which is generally consistent with the value reported for other sites dominated by silt (Soulsby, 1983; Brand et al., 2010) and is in general agreement with our estimate in **Table 2**. In the region aforementionedthe wave-current boundary layer ($z > \delta_{cw} = \kappa u_{*cw}/\omega$), the effect of the wave-current interaction is to increase the roughness experienced by the current so that the log-law becomes

$$U(z) = \frac{u_{*c}}{\kappa}\left(\frac{u_{*c}}{u_{*cw}}\log\frac{\delta_{cw}}{z_0} + \log\frac{z}{\delta_{cw}}\right). \quad (12)$$

Based on the observed data, we calculated the $u_{*c-\mathrm{GM}}$ by solving **Eqs. 10–12** iteratively. By comparison, we found that $u_{*c-\mathrm{GM}}$ was in good agreement with the results calculated by observed data ($u_{*c-\mathrm{ADV}}$) (**Supplementary Figure S2**).

Figure 13A shows the estimates C_D as a function of the ratio of bottom wave orbital velocity to mean current velocity ($u_b/\bar{u}$) during strong waves, which is a common parameter used to quantify the effect of waves (Safak, 2016). The results show that C_D increased with the increase $u_b/\bar{u}$, which is similar to the findings of Safak (2016) and Fan et al. (2019) in muddy environments. In our study, the fitted equation between C_D and $u_b/\bar{u}$ was $C_D = 0.00087\frac{u_b}{\bar{u}} + 0.00194$, $R^2 = 0.61$ (orange line in **Figure 13A**). Although bin average C_D is somewhat scattered, the R^2 is pretty good. The constant term in the fitted equation was approximately equal to the average C_D during the winter S3 and S5 observations (**Figures 11E,F**). Moreover, GM-model results (red dots in **Figure 13A**) are in good agreement with the trend of the fitted curve of observed values (orange line in **Figure 13A**). However, when we used the log-law, which does not consider wave-current interactions, the calculation C_D remained almost unchanged (black dots in **Figure 13A**). It indicates that although our observations are not within the wave's bottom boundary layer, the effect of the wave is still significant. On the one hand, waves can modify the current structure within the bottom boundary layer. We obtained the difference $\bar{u}$ calculated by log-law ($\bar{u}_{log}$) and GM-model ($\bar{u}_{GM}$) (**Figure 13B**) and found that when $u_b > 0.1 \pm 0.03$ m/s, $\bar{u}_{log} - \bar{u}_{GM}$ tended to gradually increase. On the other hand, the wave effect could lead to an enhancement of the TKE (Perlin and Kit, 2002; Bricker et al., 2005). **Figure 13C** shows the variation of TKE, which is also bounded by $u_b = 0.1 \pm 0.03$ m/s. Therefore, we infer that in the study area, $u_b \approx 0.1$ m/s can be defined as an important threshold for determining whether the wave effect is significant in the bottom boundary layer. Note that although GM-model results have the right trend, there is no good agreement between it and the observed data, especially when $u_b/\bar{u}$ is large. It indicates that under wave-current conditions similar to those in this article, the fitted equation between C_D and $u_b/\bar{u}$ could give a more accurate estimate C_D.

CONCLUSION

In situ observations of currents, waves, and suspended sediment concentration at three stations on the muddy deposits off the Shandong Peninsula was conducted to investigate the variation of the bottom drag coefficient. Data collected in both summer and winter highlight the tidal variations and the effect of winter storm events. The results show that the estimated C_D was around 0.0015 in summer and 0.0019 in winter. A significant tidal asymmetry C_D was observed in both summer and winter. By analyzing the different influencing factors one by one, we conclude that this flood–ebb asymmetry was mainly caused by the variation of local roughness; the drag reduction caused by the suspended sediment stratification was limited. Variations C_D could be affected by different hydrodynamic flow regimes. For hydrodynamically smooth flow, the bottom drag coefficient was relatively dispersed and showed an overall decrease with increase *Re*.

For hydrodynamically rough or transitional flow, the bottom drag coefficient typically was a constant that varied from 1×10^{-3} to 2.5×10^{-3} over the different observation periods. On average, hydrodynamically smooth flow occurred when *Re* was less than 2.3×10^5. In addition, strong waves, during which the bottom drag generally increases with increasing wave forcing, can lead to bias in the C_D estimates. When $u_b > 0.1 \pm 0.03$ m/s, the current-only log-law is not valid in BBL while the GMmodel performs well in terms of trends. As the waves strengthen, TKE is also significantly enhanced. In general, we believe that $u_b \approx 0.1$ m/s is the critical value to determine whether the wave effect is important in the bottom boundary layer.

In this work, we provide an accurate estimate of C_D the study area, which would be useful to improve the hydrodynamic and sediment transport models in the muddy deposits of the East China Shelf Seas. Moreover, the threshold of u_b (≈ 0.1 m/s) has guiding significance for the study of sediment transport and erosion dynamics in the bottom boundary layer. These relationships between C_D waves or currents, though based on observations off the Shandong Peninsula, could provide a reference to related research in other muddy deposits over the continental shelf.

DATA AVAILABILITY STATEMENT

The original contributions presented in the study are included in the article/**Supplementary Material**; further inquiries can be directed to the corresponding author.

AUTHOR CONTRIBUTIONS

JX and ZL: conceptualization, methodology, and reviewing. FQ: conceptualization, methodology, data curation, analyses, and original draft preparation.

FUNDING

The authors gratefully acknowledge the financial support of the Key Special Project for Introduced Talents Team of the Southern Marine Science and Engineering Guangdong Laboratory (Guangzhou) (GML2019ZD0210), Guangdong Basic and Applied Basic Research Foundation (2021B1515120080) and the National Natural Science Foundation of China (NSFC, Grant No. 41530966).

ACKNOWLEDGMENTS

Special thanks go to Baoduo Wang, Meng Liu, Zhiwen Wang, and Xiaohang Liu for their support in fieldwork.

SUPPLEMENTARY MATERIAL

The Supplementary Material for this article can be found online at: https://www.frontiersin.org/articles/10.3389/feart.2022.921995/full#supplementary-material

REFERENCES

Adams, C. E., and Weatherly, G. L. (1981). Some Effects of Suspended Sediment Stratification on an Oceanic Bottom Boundary Layer. *J. Geophys. Res.* 86 (C5), 4161–4172. doi:10.1029/JC086iC05p04161

Alexander, C. R., DeMaster, D. J., and Nittrouer, C. A. (1991). Sediment Accumulation in a Modern Epicontinental-Shelf Setting: The Yellow Sea. *Mar. Geol.* 98 (1), 51–72. doi:10.1016/0025-3227(91)90035-3

Baas, J. H., Baker, M. L., Malarkey, J., Bass, S. J., Manning, A. J., Hope, J. A., et al. (2019). Integrating Field and Laboratory Approaches for Ripple Development in Mixed Sand-Clay-EPS. *Sedimentology* 66 (7), 2749–2768. doi:10.1111/sed.12611

Bass, S. J., Aldridge, J. N., McCave, I. N., and Vincent, C. E. (2002). Phase Relationships between Fine Sediment Suspensions and Tidal Currents in Coastal Seas. *J. Geophys. Res.* 107 (C10), 3146. doi:10.1029/2001jc001269

Bian, C., Jiang, W., and Greatbatch, R. J. (2013). An Exploratory Model Study of Sediment Transport Sources and Deposits in the Bohai Sea, Yellow Sea, and East China Sea. *J. Geophys. Res. Oceans* 118 (11), 5908–5923. doi:10.1002/2013JC009116

Brand, A., Lacy, J. R., Hsu, K., Hoover, D., Gladding, S., and Stacey, M. T. (2010). Wind-enhanced Resuspension in the Shallow Waters of South San Francisco Bay: Mechanisms and Potential Implications for Cohesive Sediment Transport. *J. Geophys. Res.* 115. doi:10.1029/2010JC006172

Bricker, J. D., Inagaki, S., and Monismith, S. G. (2005). Bed Drag Coefficient Variability under Wind Waves in a Tidal Estuary. *J. Hydraul. Eng.* 131 (6), 497–508. doi:10.1061/(asce)0733-9429(2005)131:6(497)

Bricker, J. D., and Monismith, S. G. (2007). Spectral Wave-Turbulence Decomposition. *J. Atmos. Ocean. Technol.* 24 (8), 1479–1487. doi:10.1175/JTECH2066.1

Chriss, T. M., and Caldwell, D. R. (1982). Evidence for the Influence of Form Drag on Bottom Boundary Layer Flow. *J. Geophys. Res.* 87 (C6), 4148. doi:10.1029/JC087iC06p04148

Chriss, T. M., and Caldwell, D. R. (1984). Universal Similarity and the Thickness of the Viscous Sublayer at the Ocean Floor. *J. Geophys. Res.* 89 (C4), 6403–6414. doi:10.1029/JC089iC04p06403

Duan, H., Xu, J., Wu, X., Wang, H., Liu, Z., and Wang, C. (2020). Periodic Oscillation of Sediment Transport Influenced by Winter Synoptic Events, Bohai Strait, China. *Water* 12 (4), 986. doi:10.3390/w12040986

Egan, G., Chang, G., Revelas, G., Monismith, S., and Fringer, O. (2020a). Bottom Drag Varies Seasonally with Biological Roughness. *Geophys. Res. Lett.* 47 (15). doi:10.1029/2020GL088425

Egan, G., Cowherd, M., Fringer, O., and Monismith, S. (2019). Observations of Near-Bed Shear Stress in a Shallow, Wave- and Current-Driven Flow. *J. Geophys. Res. Oceans* 124 (8), 6323–6344. doi:10.1029/2019JC015165

Egan, G., Manning, A. J., Chang, G., Fringer, O., and Monismith, S. (2020b). Sediment-Induced Stratification in an Estuarine Bottom Boundary Layer. *J. Geophys. Res. Oceans* 125 (8). doi:10.1029/2019JC016022

Fan, R., Zhao, L., Lu, Y., Nie, H., and Wei, H. (2019). Impacts of Currents and Waves on Bottom Drag Coefficient in the East China Shelf Seas. *J. Geophys. Res. Oceans* 124 (11), 7344–7354. doi:10.1029/2019JC015097

Feddersen, F., Gallagher, E. L., Guza, R. T., and Elgar, S. (2003). The Drag Coefficient, Bottom Roughness, and Wave-Breaking in the Nearshore. *Coast. Eng.* 48 (3), 189–195. doi:10.1016/s0378-3839(03)00026-7

Feddersen, F., and Williams, A. J. (2007). Direct Estimation of the Reynolds Stress Vertical Structure in the Nearshore. *J. Atmos. Ocean. Technol.* 24 (1), 102–116. doi:10.1175/JTECH1953.1

Fong, D. A., Monismith, S. G., Stacey, M. T., and Burau, J. R. (2009). Turbulent Stresses and Secondary Currents in a Tidal-Forced Channel with Significant Curvature and Asymmetric Bed Forms. *J. Hydraul. Eng.* 135 (3), 198–208. doi:10.1061/(asce)0733-9429(2009)135:3(198)

Francis P. Shepard, F. P. (1954). Nomenclature Based on Sand-Silt-Clay Ratios. *Sepm Jsr* Vol. 24 (3), 151–158. doi:10.1306/d4269774-2b26-11d7-8648000102c1865d

Fringer, O. B., Dawson, C. N., He, R., Ralston, D. K., and Zhang, Y. J. (2019). The Future of Coastal and Estuarine Modeling: Findings from a Workshop. *Ocean. Model.* 143, 101458. doi:10.1016/j.ocemod.2019.101458

Grant, W. D., and Madsen, O. S. (1979). Combined Wave and Current Interaction with a Rough Bottom. *J. Geophys. Res.* 84 (C4), 1797–1808. doi:10.1029/JC084iC04p01797

Grant, W. D., and Madsen, O. S. (1986). The Continental-Shelf Bottom Boundary Layer. *Annu. Rev. Fluid Mech.* 18 (1), 265–305. doi:10.1146/ANNUREV.FL.18.010186.001405

Green, M. O., and Mccave, I. N. (1995). Seabed Drag Coefficient under Tidal Currents in the Eastern Irish Sea. *J. Geophys. Res.* 100 (C8), 16057–16069. doi:10.1029/95JC01381

Harris, C. K., and Wiberg, P. L. (2001). A Two-Dimensional, Time-dependent Model of Suspended Sediment Transport and Bed Reworking for Continental Shelves. *Comput. Geosciences* 27 (6), 675–690. doi:10.1016/S0098-3004(00)00122-9

Herrmann, M. J., and Madsen, O. S. (2007). Effect of Stratification Due to Suspended Sand on Velocity and Concentration Distribution in Unidirectional Flows. *J. Geophys. Res.* 112 (C2). doi:10.1029/2006jc003569

Jones, N. L., and Monismith, S. G. (2008). Modeling the Influence of Wave-Enhanced Turbulence in a Shallow Tide- and Wind-Driven Water Column. *J. Geophys. Res.* 113, 1–13. doi:10.1029/2007JC004246

Kaimal, J. C., Wyngaard, J. C., Izumi, Y., and Coté, O. R. (1972). Spectral Characteristics of Surface-Layer Turbulence. *Q.J R. Met. Soc.* 98 (417), 563–589. doi:10.1002/QJ.49709841707

Liu, S., Qiao, L., Li, G., Li, J., Wang, N., and Yang, J. (2015). Distribution and Cross-Front Transport of Suspended Particulate Matter over the Inner Shelf of the East China Sea. *Cont. Shelf Res.* 107, 92–102. doi:10.1016/j.csr.2015.07.013

Liu, Z., and Wei, H. (2007). Estimation to the Turbulent Kinetic Energy Dissipation Rate and Bottom Shear Stress in the Tidal Bottom Boundary Layer of the Yellow Sea. *Progress in Natural Science* 17, 289–297. doi:10.1080/10020070612331343260

MacVean, L. J., and Lacy, J. R. (2014). Interactions between Waves, Sediment, and Turbulence on a Shallow Estuarine Mudflat. *J. Geophys. Res. Oceans* 119 (3), 1534–1553. doi:10.1002/2013JC009477

Magaldi, M. G., Özgökmen, T. M., Griffa, A., and Rixen, M. (2009). On the Response of a Turbulent Coastal Buoyant Current to Wind Events: the Case of the Western Adriatic Current. *Ocean. Dyn.* 60 (1), 93–122. doi:10.1007/s10236-009-0247-9

Mo, D., Hou, Y., Li, J., and Liu, Y. (2016). Study on the Storm Surges Induced by Cold Waves in the Northern East China Sea. *J. Mar. Syst.* 160, 26–39. doi:10.1016/j.jmarsys.2016.04.002

Naimie, C. E., Blain, C. A., and Lynch, D. R. (2001). Seasonal Mean Circulation in the Yellow Sea } a Model-Generated Climatology. *Cont. Shelf Res.* 21 (6), 667–695. doi:10.1016/S0278-4343(00)00102-3

Nayak, A. R., Li, C., Kiani, B. T., and Katz, J. (2015). On the Wave and Current Interaction with a Rippled Seabed in the Coastal Ocean Bottom Boundary Layer. *J. Geophys. Res. Oceans* 120 (7), 4595–4624. doi:10.1002/2014jc010606

Nelson, K. S., and Fringer, O. B. (2018). Sediment Dynamics in Wind Wave-Dominated Shallow-Water Environments. *J. Geophys. Res. Oceans* 123 (10), 6996–7015. doi:10.1029/2018jc013894

Pawlowicz, R., Beardsley, B., and Lentz, S. (2002). Classical Tidal Harmonic Analysis Including Error Estimates in MATLAB Using T_TIDE. *Comput. Geosciences* 28 (8), 929–937. doi:10.1016/S0098-3004(02)00013-4

Peng, Y., Yu, Q., Yang, Y., Wang, Y., Wang, Y. P., and Gao, S. (2020). Flow Structure Modification and Drag Reduction Induced by Sediment Stratification in Coastal Tidal Bottom Boundary Layers. *Estuar. Coast. Shelf Sci.* 241, 106829. doi:10.1016/j.ecss.2020.106829

Perlin, A., and Kit, E. (2002). Apparent Roughness in Wave-Current Flow: Implication for Coastal Studies. *J. Hydraul. Eng.* 128 (8), 729–741. doi:10.1061/(asce)0733-9429(2002)128:8(729)

Peters, H. (1999). Spatial and Temporal Variability of Turbulent Mixing in an Estuary. *J. Mar. Res.* 57 (6), 805–845. doi:10.1357/002224099321514060

Qi, F., Wu, X., Wang, Z., Wang, C., Duan, H., Liu, M., et al. (2022). Transport and Deposition Processes of the Sediment Depocenter off the Shandong Peninsula: An Observational Study. *Cont. Shelf Res.* 244, 104763. doi:10.1016/j.csr.2022.104763

Ruessink, B. G. (2010). Observations of Turbulence within a Natural Surf Zone. *J. Phys. Oceanogr.* 40 (12), 2696–2712. doi:10.1175/2010jpo4466.1

Safak, I. (2016). Variability of Bed Drag on Cohesive Beds under Wave Action. *Water* 8 (4), 131. doi:10.3390/w8040131

Saha, S., Moorthi, S., Wu, X., Wang, J., Nadiga, S., Tripp, P., et al. (2014). The NCEP Climate Forecast System Version 2. *J. Clim.* 27 (6), 2185–2208. doi:10.1175/JCLI-D-12-00823.1

Scully, M. E., Trowbridge, J. H., Sherwood, C. R., Jones, K. R., and Traykovski, P. (2018). Direct Measurements of Mean Reynolds Stress and Ripple Roughness in the Presence of Energetic Forcing by Surface Waves. *J. Geophys. Res. Oceans* 123 (4), 2494–2512. doi:10.1002/2017jc013252

Sherwood, C. R., Lacy, J. R., and Voulgaris, G. (2006). Shear Velocity Estimates on the Inner Shelf off Grays Harbor, Washington, USA. *Cont. Shelf Res.* 26 (17-18), 1995–2018. doi:10.1016/j.csr.2006.07.025

Signell, R. P., and List, J. H. (1997). Effect of Wave-Enhanced Bottom Friction on Storm-Driven Circulation in Massachusetts Bay. *J. Waterw. Port Coast. Ocean Eng.* 123 (5), 233–239. doi:10.1061/(asce)0733-950x(1997)123:5(233)

Soulsby, R. L. (1983). Chapter 5 the Bottom Boundary Layer of Shelf Seas. *Elsevier Oceanogr.* 35, 189–266. doi:10.1016/S0422-9894(08)70503-8

Soulsby, R. L., and Dyer, K. R. (1981). The Form of the Near-Bed Velocity Profile in a Tidally Accelerating Flow. *J. Geophys. Res.* 86 (C9), 8067–8074. doi:10.1029/JC086iC09p08067

Soulsby, R. L. (2006). *Simplified Calculation of Wave Orbital Velocities*. Wallingford: HR Wallingford Ltd.

Soulsby, R. L. (1997). *The Dynamics of Marine Sands: A Manual for Practical Applications*. London: Thomas Thelford.

Sreenivasan, K. R., and Katepalli, R. (1995). On the Universality of the Kolmogorov Constant. *Phys. Fluids* 7 (11), 2778–2784. doi:10.1063/1.868656

Sternberg, R. W. (1970). Field Measurements of the Hydrodynamic Roughness of the Deep-Sea Boundary. *Deep Sea Res. Oceanogr. Abstr.* 17 (3), 413–420. doi:10.1016/0011-7471(70)90056-2

Sternberg, R. W. (1968). Friction Factors in Tidal Channels with Differing Bed Roughness. *Mar. Geol.* 6 (3), 243–260. doi:10.1016/0025-3227(68)90033-9

Styles, R., and Glenn, S. M. (2000). Modeling Stratified Wave and Current Bottom Boundary Layers on the Continental Shelf. *J. Geophys. Res.* 105 (C10), 24119–24139. doi:10.1029/2000jc900115

Teague, W. J., Perkins, H. T., Hallock, Z. R., and Jacobs, G. A. (1998). Current and Tide Observations in the Southern Yellow Sea. *J. Geophys. Res.* 103 (C12), 27783–27793. doi:10.1029/98jc02672

Tolman, H. L., Accensi, M., Alves, H., Ardhuin, F., Bidlot, J., Booij, N., et al. (2014). *User Manual and System Documentation of WAVEWATCH III R Version 4.18*.

Trembanis, A. C., Wright, L. D., Friedrichs, C. T., Green, M. O., and Hume, T. (2004). The Effects of Spatially Complex Inner Shelf Roughness on Boundary Layer Turbulence and Current and Wave Friction: Tairua Embayment, New Zealand. *Cont. Shelf Res.* 24 (13-14), 1549–1571. doi:10.1016/j.csr.2004.04.006

Trowbridge, J. H., and Lentz, S. J. (2018). The Bottom Boundary Layer. *Annu. Rev. Mar. Sci.* 10, 397–420. doi:10.1146/annurev-marine-121916-063351

Tu, J., Fan, D., and Voulgaris, G. (2021). Field Observations of Turbulence, Sediment Suspension, and Transport under Breaking Tidal Bores. *Mar. Geol.* 437, 106498. doi:10.1016/j.margeo.2021.106498

Tu, J., Fan, D., Zhang, Y., and Voulgaris, G. (2019). Turbulence, Sediment-Induced Stratification, and Mixing under Macrotidal Estuarine Conditions (Qiantang Estuary, China). *J. Geophys. Res. Oceans* 124 (6), 4058–4077. doi:10.1029/2018jc014281

Van Rijn, L. C. (1993). *Principles of Sediment Transport in Rivers, Estuaries and Coastal Seas Part 1*. Amsterdam: Aqua Publications.

Van Rijn, L. C. (2007). Unified View of Sediment Transport by Currents and Waves. I: Initiation of Motion, Bed Roughness, and Bed-Load Transport. *J. Hydraul. Eng.* 133 (6), 649–667. doi:10.1061/(asce)0733-9429(2007)133:6(649)

Vieira da Silva, G., Toldo Jr., E. E., Klein, A. H. d. F., and Short, A. D. (2018). The Influence of Wave-, Wind- and Tide-Forced Currents on Headland Sand Bypassing - Study Case: Santa Catarina Island North Shore, Brazil. *Geomorphology* 312, 1–11. doi:10.1016/J.GEOMORPH.2018.03.026

Wang, A., Ralston, D. K., Bi, N., Cheng, Z., Wu, X., and Wang, H. (2019). Seasonal Variation in Sediment Transport and Deposition on a Muddy Clinoform in the Yellow Sea. *Cont. Shelf Res.* 179, 37–51. doi:10.1016/j.csr.2019.04.009

Wang, C., Liu, Z., Harris, C. K., Wu, X., Wang, H., Bian, C., et al. (2020). The Impact of Winter Storms on Sediment Transport through a Narrow Strait, Bohai, China. *J. Geophys. Res. Oceans* 125 (6), e2020JC016069. doi:10.1029/2020jc016069

Wang, D., Liu, Q., and Lv, X. (2014). A Study on Bottom Friction Coefficient in the Bohai, Yellow, and East China Sea. *Math. Problems Eng.* 2014, 1–7. doi:10.1155/2014/432529

Warner, J. C., Sherwood, C. R., Signell, R. P., Harris, C. K., and Arango, H. G. (2008). Development of a Three-Dimensional, Regional, Coupled Wave, Current, and Sediment-Transport Model. *Comput. Geosciences* 34 (10), 1284–1306. doi:10.1016/j.cageo.2008.02.012

Wiberg, P. L., and Sherwood, C. R. (2008). Calculating Wave-Generated Bottom Orbital Velocities from Surface-Wave Parameters. *Comput. Geosciences* 34 (10), 1243–1262. doi:10.1016/j.cageo.2008.02.010

Wilkinson, R. H. (1985). Variation of Roughness Length of a Mobile Sand Bed in a Tidal Flow. *Geo-Marine Lett.* 5 (4), 231–239. doi:10.1007/BF02233808

Wright, L. D. (1989). Benthic Boundary Layers of Estuarine and Coastal Environments. *Rev. Aquatic Sci.* 1, 75–95.

Wright, L. D., Kim, S. C., and Friedrichs, C. T. (1999). Across-shelf Variations in Bed Roughness, Bed Stress and Sediment Suspension on the Northern California Shelf. *Mar. Geol.* 154 (1), 99–115. doi:10.1016/S0025-3227(98)00106-6

Wu, H., Wang, Y. P., Gao, S., Xing, F., Tang, J., and Chen, D. (2022). Fluid Mud Dynamics in a Tide-Dominated Estuary: A Case Study from the Yangtze River. *Cont. Shelf Res.* 232, 104623. doi:10.1016/j.csr.2021.104623

Wu, X., Xu, J., Wu, H., Bi, N., Bian, C., Li, P., et al. (2019). Synoptic Variations of Residual Currents in the Huanghe (Yellow River)-Derived Distal Mud Patch off the Shandong Peninsula: Implications for Long-Term Sediment Transport. *Mar. Geol.* 417, 106014. doi:10.1016/j.margeo.2019.106014

Xu, J. P., and Wright, L. D. (1995). Tests of Bed Roughness Models Using Field Data from the Middle Atlantic Bight. *Cont. Shelf Res.* 15, 1409–1434. doi:10.1016/0278-4343(94)00083-Y

Xu, P., Mao, X., and Jiang, W. (2017). Estimation of the Bottom Stress and Bottom Drag Coefficient in a Highly Asymmetric Tidal Bay Using Three Independent Methods. *Cont. Shelf Res.* 140, 37–46. doi:10.1016/j.csr.2017.04.004

Yang, Z. S., and Liu, J. P. (2007). A Unique Yellow River-Derived Distal Subaqueous Delta in the Yellow Sea. *Mar. Geol.* 240 (1-4), 169–176. doi:10.1016/j.margeo.2007.02.008

Yuan, P., Wang, H., Wu, X., and Bi, N. (2020). Grain-Size Distribution of Surface Sediments in the Bohai Sea and the Northern Yellow Sea: Sediment Supply and Hydrodynamics. *J. Ocean. Univ. China* 19 (3), 589–600. doi:10.1007/s11802-020-4221-y

Conflict of Interest: The authors declare that the research was conducted in the absence of any commercial or financial relationships that could be construed as a potential conflict of interest.

Publisher's Note: All claims expressed in this article are solely those of the authors and do not necessarily represent those of their affiliated organizations, or those of the publisher, the editors, and the reviewers. Any product that may be evaluated in this article, or claim that may be made by its manufacturer, is not guaranteed or endorsed by the publisher.